ACS APPLIED ENERGY MATERIALS

www.acsaem.org Article

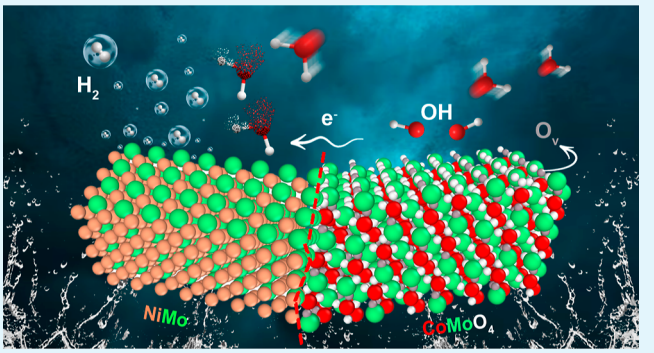
NiMo/$CoMoO_4$ Heterostructure with Confined Oxygen Vacancy for Active and Durable Alkaline Hydrogen Evolution Reaction

Ebrahim Sadeghi, Sanaz Chamani, Emre Erdem, Naeimeh Sadat Peighambardoust, and Umut Aydemir*

Cite This: *ACS Appl. Energy Mater.* 2023, 6, 7658−7671 Read Online

ACCESS | Metrics & More | Article Recommendations | Supporting Information

ABSTRACT: The sluggish kinetics of electrocatalysts in the alkaline hydrogen evolution reaction (HER) is a critical challenge to attain efficient progress in water electrolysis for carbon-neutral hydrogen production. Here, we present a high-performance and durable heterostructure of NiMo/$CoMoO_4$ for the alkaline HER constructed via a two-pot in situ growth strategy on a nickel foam (NF). The density of active sites and the surface area of the hybrid catalyst augmented almost three-fold compared to those of pristine $CoMoO_4$. The heterostructure composed of metallic NiMo and oxygen vacancy (O_v)-confined $CoMoO_4$ facilitated the H adsorption on the metallic side and OH adsorption on the oxide side. The hierarchical hybrid catalyst on NF featured a low overpotential of 102 mV at 10 mA cm^{-2}, approaching that of platinum on carbon (83 mV) in 1.0 M KOH. The turnover frequency of 0.012 s^{-1} at the overpotential of 100 mV of NiMo/$CoMoO_4$ is six times higher than that of $CoMoO_4$, 0.002 s^{-1}. In addition, the fabricated heterostructure is a highly durable HER catalyst at 30 mA cm^{-2} for 30 h. The Faradaic efficiency recorded by a gas chromatograph at 10 and 100 mA cm^{-2} revealed nearly 100 and 86−95% hydrogen production efficiency, respectively.



KEYWORDS: *electrocatalysis, hydrogen evolution reaction, oxygen vacancy, metal oxides, heterostructure*

Downloaded via KOC UNIV on February 19, 2025 at 07:21:50 (UTC).
See https://pubs.acs.org/sharingguidelines for options on how to legitimately share published articles.

1. INTRODUCTION

As the world faces a looming shortage of fossil fuels, research into developing alternative clean energy sources has been ramping up.[1,2] The production of high-purity hydrogen through the use of renewable energy sources via electrochemical water splitting is a promising solution for sustainable energy production.[3−5] The process of electrochemical water splitting catalyzed by specialized materials requires two distinct reactions to occur, the hydrogen evolution reaction (HER) at the cathode, i.e.

$$2H_2O + 2e^- \rightarrow H_2 + 2OH^- \quad (R1)$$

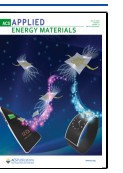
and the oxygen evolution reaction (OER) at the anode, i.e.[6]

$$4OH^- \rightarrow O_2 + 2H_2O + 4e^- \quad (R2)$$

In this context, the generation of hydrogen specifically has significant value in terms of its utilization in the energy industry. To achieve this goal, researchers have been working tirelessly to create low-cost, long-lasting, and effective electrode materials that can efficiently produce hydrogen in an alkaline environment.[7−9]

So far, a variety of materials derived from transition metals (TMs) have been explored as high-efficiency electrocatalysts for HER and/or OER.[10−15] Among TM derivatives, TM oxides (TMOs) possess several benefits, such as high electrochemical activities, enhanced electronic conductivity in some cases—as a result of their multiple oxidation states at interfaces—, and relatively low activation energy for electron transfer between cations.[16] In principle, hydrogen evolution in alkaline solutions consists of two steps: (i) adsorption of water to split into H* and OH* intermediates (Volmer step), followed by (ii) combination of H* intermediates to form H_2 and its desorption from the surface (Heyrovsky or Tafel step).[17,18] In addition, the Gibbs free energy (ΔG_{H^*}) of hydrogen adsorption at the active site is an index to determine the HER performance of catalysts.[17] Therefore, the closer the values of ΔG_{H^*} to zero, the higher the hydrogen adsorption/desorption efficiency. Because of the exceptional water adsorption performance exhibited by molybdenum in the HER, many studies have concentrated on incorporating other elements into it,[17] including NiMo, CoMo, and MnMo, to control the desorption ability of water at the catalyst surface. In addition, Co-based and Mo-based oxides have gained

Received: May 5, 2023
Accepted: June 20, 2023
Published: July 10, 2023



© 2023 The Authors. Published by American Chemical Society

increasing interest as potential low-cost electrochemical catalysts due to their electronic structure among various metal oxides.[19]

Metal molybdates, a significant class of inorganic materials, have possible uses in various areas, such as catalysis, magnetic applications, humidity sensing, photoluminescence, and energy storage.[20−22] $CoMoO_4$, a member of the metal molybdates family, has been found to enjoy compelling properties, including nontoxicity, unique crystal structure, multiple valence states, and ability to reversibly store small ions, which makes it a favorable choice as an electrode material.[20,21] However, the poor electrical conductivity of $CoMoO_4$ and the limited number of active sites are the reasons for its unsatisfactory HER performance in alkaline media. To improve the electrocatalytic character of $CoMoO_4$ for the HER, various research methods have been employed to boost electron transfer and increase the number of active sites. These methods include modifying the electronic structure of $CoMoO_4$ by introducing element dopants, heterostructure engineering, controlling the crystal facets, and creating oxygen vacancies.[17,23]

The HER performances of Pt-based catalysts under alkaline conditions are determined by their capacity to bind hydroxyl species (OH*),[24,25] and the optimization of the alkaline HER process can be attained by regulating the binding energies of reactants (OH* and H*) on dual active sites.[26−28] A similar analogy can be evinced for TM-based catalysts to minimize the kinetic barrier of the Volmer step in alkaline media by adding or designing dual active sites in the catalyst to separately fine-tune the binding energy (BE) of reactants (OH* and H*). One way to address this issue is to develop catalysts that combine metals and metal oxides. These catalysts can cleave the H−OH bond with the help of oxides, while the metal component helps to adsorb and recombine the resulting H* intermediates into molecules. According to the calculations performed by Zhou et al.[18] using density functional theory (DFT), it was shown that the dual active sites at the interfaces of the NiO/Ni heterostructure—consisting of metallic Ni sites and oxygen vacancy-modified NiO sites—have adsorption preference toward H* and OH*, individually, facilitating the water adsorption and alleviating the water cleavage with a lower energy barrier of 0.31 eV in Volmer step for the NiO/Ni heterostructure compared to those of the individual components of Ni (0.47 eV) and NiO (1.42 eV) catalysts.[18] Moreover, oxygen vacancies can act as electron donors (n-type defects) and accelerate the electron transfer process. Furthermore, oxygen vacancies can modify the electronic structure of metal oxides, thereby improving their electrical conductivity.[29]

Herein, we combined oxygen vacancy-confined $CoMoO_4$ with NiMo alloy nanoparticles (NPs) to facilitate water adsorption and boost the HER performance of the resultant heterostructure in alkaline conditions. Ni-based materials have gained popularity as electrocatalysts for alkaline HER because of the energy required for hydrogen binding, which is closer to that of Pt.[30] Furthermore, open literature has shown that alloying Ni with other metals such as Ru,[31] Cu,[32] Zn,[33] Fe, Co, and Mo can further boost the catalyst's activity for HER owing to their synergistic optimization of active edge sites and excellent corrosion resistance to the basic environment.[34,35] NiMo alloys, however, have been found to be particularly effective for HER due to their intrinsic activity and favorable hydrogen BE.[36] Yet, the overall performance of NiMo alloy alone is not optimal, resulting in low efficiency and high energy consumption. Thus, it is of utmost importance to promote the catalytic behavior of NiMo alloy.[36] Besides heterostructure engineering, a different approach is to enhance the HER performance by increasing the specific surface area. To do so, researchers have utilized various substrates as supports for NiMo alloy electrodes with high specific areas such as the Ni foam (NF), Cu foam, carbon cloth, and Ti mesh.[37,38] In this study, a heterostructure, composed of a metallic-like component (NiMo alloy) and an oxide ($CoMoO_4$), was fabricated directly on an NF substrate. The NiMo/$CoMoO_4$@NF reached 10 mA cm^{-2} at a low overpotential of 102 mV in a 1.0 M KOH solution.

In general, the superior activity of the NiMo/$CoMoO_4$ catalyst toward HER could be attributed to one or more of the following factors: (i) the large number of active sites correlated with the electrochemically active surface area (ECSA) and the specific surface area determined by Brunauer−Emmett−Teller (BET) analysis; both ECSA and BET surface areas grew three-fold larger compared to those of $CoMoO_4$, (ii) proper regulation of the binding ability of the intermediates (OH* and H*) with active sites; metallic-like NiMo has adsorption affinity toward H*, while the oxygen vacancy-confined $CoMoO_4$ has adsorption affinity toward OH*, leading to higher intrinsic activity compared to that of single components, (iii) appropriate interface engineering can enhance electron transfer and redistribution; for this, unique atomic coordination at the interface of NiMo NPs and $CoMoO_4$ can significantly affect the electrocatalytic HER. Once NiMo is combined with $CoMoO_4$, the interface of the heterostructure is expected to experience an electronic redistribution due to varying electronegativities of the atoms involved (3.44 for O atom, 1.91 for Ni, 1.88 for Co, and 2.16 for Mo).

2. EXPERIMENTAL SECTION

2.1. Catalyst Preparation. *2.1.1. Materials.* Polyvinylpyrrolidone (PVP, Sigma-Aldrich), nickel chloride hexahydrate ($NiCl_2{\cdot}6H_2O$, Sigma-Aldrich, 99.9% trace metals basis), sodium molybdate dihydrate ($Na_2MoO_4{\cdot}2H_2O$, Sigma-Aldrich, ACS reagent, ≥99%), sodium borohydride ($NaBH_4$, Sigma-Aldrich), and cobalt nitrate hexahydrate [$Co(NO_3)_2{\cdot}6H_2O$, Sigma-Aldrich, 99.999% trace metals basis] were purchased and used without any prior treatment.

2.1.2. Synthesis of NiMo NPs. The method used to synthesize NiMo alloy NPs followed a previously reported surfactant-aided co-reduction process,[39] with some minor modifications. To briefly summarize, 1 g of PVP was dissolved in 50 mL of deionized (DI) water to obtain a clear, colorless solution. Then, 356 mg of $NiCl_2{\cdot}6H_2O$ (1.5 mmol) and 120 mg of $Na_2MoO_4{\cdot}2H_2O$ (0.5 mmol) were added to the PVP-containing solution and dissolved via vigorous stirring—a nominal composition of 3:1 for Ni/Mo. After 30 min, 200 mg of $NaBH_4$ was quickly added into the above mixture solution, and the reaction mixture was stirred vigorously until the formation of bubbles stopped. The resulting black suspension was rinsed with DI water and pure ethanol repeatedly and then vacuum-dried at 100 °C for 24 h. For better understanding the crystallinity of the obtained NiMo NPs, the ground powder was transferred into an alumina crucible and then inserted into a homemade tubular quartz tube. The tube was then placed in a tubular furnace and heated under an Ar atmosphere at 550 °C for 3 h.

2.1.3. Synthesis of NiMo/$CoMoO_4$@NF. The commercial NF (1.5 cm × 3 cm) was treated by ultrasonication with 2.0 M HCl solution, acetone, DI water, and ethanol, each for 10 min to remove the contaminants, such as oxide from the NF surface, and dried by exposing it to the open air. For the fabrication of $CoMoO_4$ on NF, 2 mmol of $Co(NO_3)_2{\cdot}6H_2O$ and 2 mmol of $Na_2MoO_4{\cdot}2H_2O$ were

https://doi.org/10.1021/acsaem.3c01146
ACS Appl. Energy Mater. 2023, 6, 7658−7671

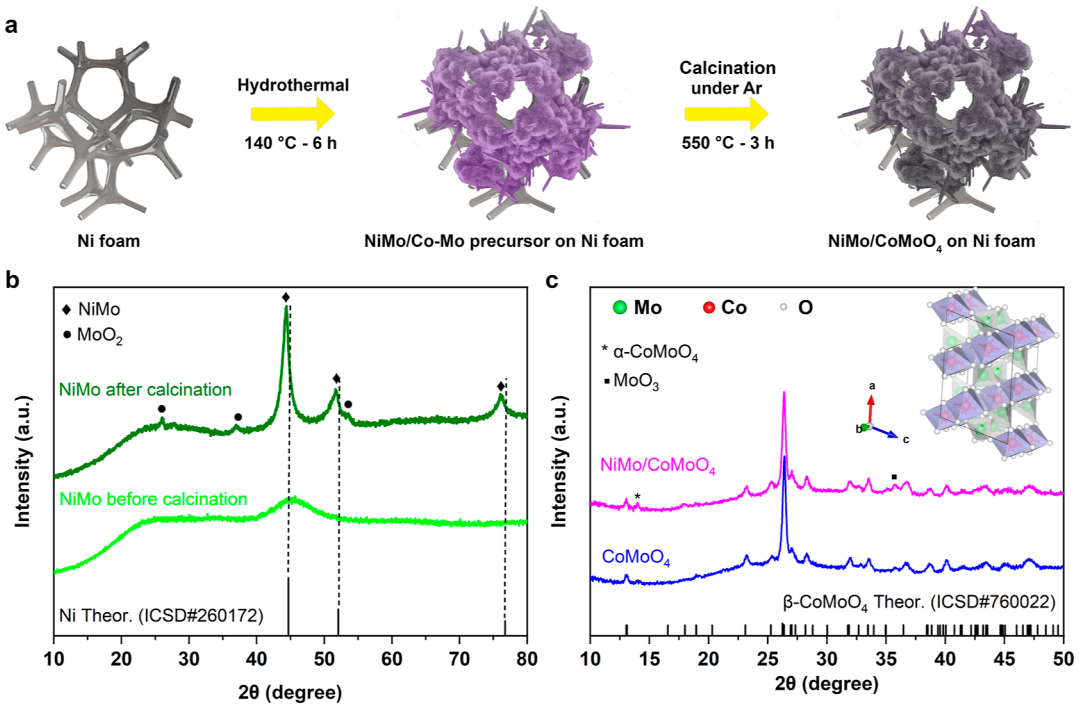


Figure 1. (a) Schematic illustration of the preparation procedure of the NiMo/$CoMoO_4$ heterostructure, (b) XRD patterns of NiMo NPs before and after heat treatment at 550 °C under Ar, and (c) XRD patterns of pristine β-$CoMoO_4$ and NiMo/$CoMoO_4$ (inset: crystal structure of $CoMoO_4$).

dissolved in 40 mL DI water. The ingredients were mixed by stirring at room temperature until a clear, deep red solution was formed. A specified quantity of already prepared powder of NiMo NPs (20 wt %) was added to the solution mixture and stirred for 60 min. The solution was subjected to ultrasonic vibrations for an additional 60 min. The prepared mixture was then poured into a 50 mL Teflon-lined stainless steel autoclave, and the previously cleaned NF was added to it. The autoclave was tightly sealed and placed in an oven, where it was kept at 140 °C for 6 h. After being allowed to cool down to room temperature naturally, the Co−Mo precursor coated on the NF was washed with DI water and pure ethanol and then vacuum-dried overnight at 60 °C. Finally, the NF coated with Co−Mo precursor/NiMo was put into an alumina crucible, and the same calcination step was performed for 3 h at 550 °C under Ar flow. The NiMo/$CoMoO_4$ on NF was obtained after the product was cooled to room temperature under Ar flow (see the schematic illustration in Figure 1a). $CoMoO_4$ on the NF substrate was synthesized by the same process but without NiMo addition to the solution prior to the hydrothermal step.

2.1.4. Preparation of Pt/C@NF. According to our previous study,[40] 1 mg of commercial 20% Pt/C was ultrasonically dispersed in a solution of pure ethanol (300 μL) and DI water (200 μL) for 30 min. Afterward, 10 μL of Nafion solution was added and sonicated for another 30 min to gain a homogeneous ink solution. The prepared ink was pipetted onto a piece of NF to obtain a mass loading of approximately 1 mg cm^{-2}.

2.2. Materials Characterization. The crystal phase and purity of the products were analyzed by X-ray diffraction (XRD, Rigaku Mini Flex 600, Cu Kα radiation, λ = 1.5418 Å). The morphology was investigated by a field-emission scanning electron microscope (FE-SEM) Zeiss Ultra Plus) equipped with an energy-dispersive X-ray spectroscopy (EDS) detector (Bruker XFlash 5010, 123 eV spectral resolution). The microstructure, selected area electron diffraction (SAED), and lattice fringes were further studied by high-resolution transmission electron microscopy (HR-TEM; Thermo Scientific Talos F200S 200 kV). In addition, high-angle annular dark-field scanning transmission electron microscopy (HAADF-STEM) images and the associated EDS-STEM mappings were obtained using a microscope (Hitachi HF5000 200 kV (S)TEM, working in HR mode). The surface composition and oxidation states were obtained by X-ray photoelectron spectroscopy (XPS, Thermo Scientific K-Alpha with an Al Kα monochromator source, 1486.6 eV). All XPS spectra were corrected according to the BE of C 1s = 284.50 eV. The vibrational modes of molecules were monitored by Raman spectroscopy (Raman microscope, RENISHAW INVIA, 532 nm excitation laser source). The functional groups were identified by Fourier transform-infrared (FT-IR) spectroscopy (JASCO 6800 full vacuum and FT-IR microscope). X-band (9.65 GHz) electron paramagnetic resonance (EPR) measurements were performed at room temperature with a Bruker EMXnano. The offset in the magnetic field and the exact g-factors in X-band measurements were determined with a polycrystalline DPPH (2-diphenyl-1-picrylhydrazyl) reference sample with a well-known g-factor (g = 2.0036). The BET-specific surface area was determined through N_2 adsorption−desorption isotherms (Micromeritics ASAP 2010). Finally, inductively coupled plasma-mass spectrometry (ICP-MS, Agilent 7700x) was employed to check the possibility of the Pt spring—the counter electrode—dissolution in the alkaline condition after the post-stability test.

2.3. Electrochemical Characterization. All electrochemical experiments were performed with an AutoLab Potentiostat Galvanostat (PGSTAT302N, the Netherlands) in a standard three-electrode system in an alkaline solution (1.0 M KOH). A reversible hydrogen electrode (RHE; HydroFlex) was used as the reference electrode, and a Pt spring was employed as the counter electrode. The catalysts grown on the NF (0.5 cm × 1 cm) were utilized as the working electrodes. The linear sweep voltammetry (LSV) curves were recorded in the HER potential region (0 to −1 V) at a scan rate of 5 mV s^{-1}. The HER overpotentials were considered at current densities of 10 and 50 mA cm^{-2}. The recorded LSV curves were then replotted to receive Tafel plots. The ECSA was acquired through the double-layer capacitance (C_{dl}) with respect to the cyclic voltammetry (CV) measured at various scan rates of 0.02, 0.04, 0.06, 0.08, 0.1, and 0.12 V s^{-1} across the potential window from 0.75 to 0.85 V vs RHE. The turnover frequency (TOF) was determined with a consistent interval of 100 mV, within a defined overpotential range of 100−500 mV. The long-term HER stability was performed through a

https://doi.org/10.1021/acsaem.3c01146
ACS Appl. Energy Mater. 2023, 6, 7658−7671

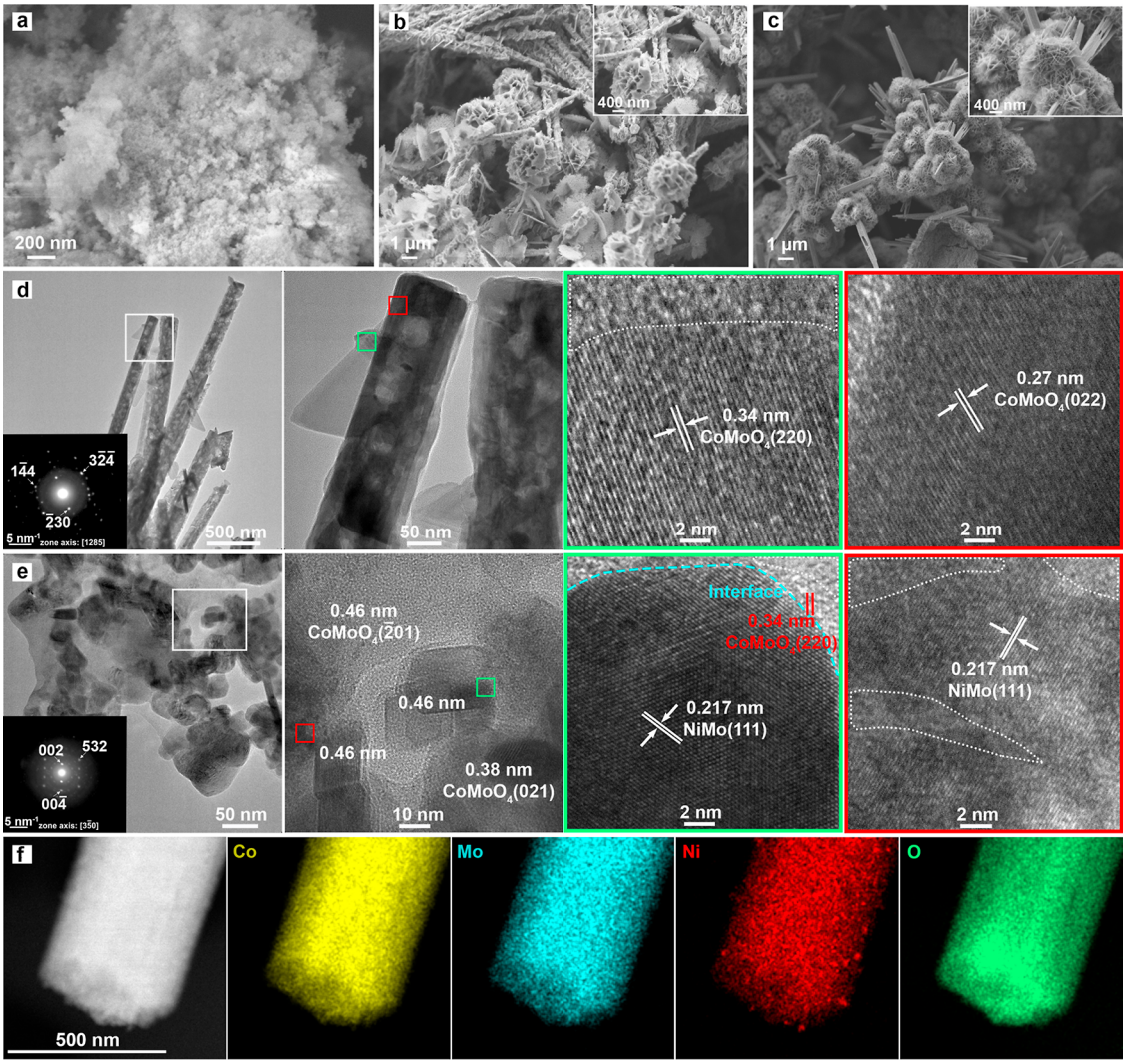


Figure 2. Morphological and microstructural characterizations of the samples. SEM images of (a) NiMo NPs before heat treatment, (b) pristine $CoMoO_4$, and (c) NiMo/$CoMoO_4$ (inset: high-magnification SEM images). (d) TEM photographs related to pristine $CoMoO_4$ (inset: SAED pattern); white square shows the high-magnification TEM images of nanorods, and green and red squares show the HR-TEM images of the lattice spacing of $CoMoO_4$. (e) TEM photographs related to NiMo/$CoMoO_4$ (inset: SAED pattern); white square shows the high-magnification TEM images of $CoMoO_4$ nanosheets along with NiMo NPs, green square shows an interface in the heterostructure, red square shows HR-TEM images of NiMo lattice spacing within the heterostructure (the enclosed irregular-shaped dotted regions show the lattice distortion as a result of oxygen vacancy). (f) HAADF−STEM image and the corresponding EDS−STEM mappings of NiMo/$CoMoO_4$.

chronopotentiometry test at an applied current density of 30 mA cm^{-2} for 30 h. The electrochemical impedance spectroscopy (EIS) measurements were performed at 0.0 V vs RHE over a frequency region of 100 kHz to 0.1 Hz. To better study HER kinetics, the EIS experiments were carried out at 100−200 mV vs RHE at a regular interval of 10 mV. All the electrochemical data were presented without iR correction as the uncompensated resistance was calculated to be 11.7 Ω. The obtained value was introduced to the electrochemical measurements, and it had almost no impact on the results. Finally, hydrogen gas production was detected and quantified using a gas chromatograph (7820A, GC System, Agilent) equipped with a thermal conductivity detector (TCD). The experiment was conducted in a tightly sealed cell to ensure accuracy, and a three-electrode configuration system was employed, consistent with the electrochemical characterizations.

3. RESULTS AND DISCUSSION

3.1. Chemical Studies. XRD characterization was employed to examine the phase structure of NiMo NPs, $CoMoO_4$, and NiMo/$CoMoO_4$. As shown in Figure 1b, NiMo before heat treatment shows only one broad peak at around 2θ = 45°, demonstrating its amorphous nature, which is common for NiMo alloys with various compositions.[7,39] On the flip side, we can see a highly crystalline phase after heat treatment at 550 °C. It is noticed that the representative peaks of Ni in NiMo shifted to the lower 2θ values relative to the XRD pattern of reference Ni (ICSD code no. 260172), indicating the formation of an alloy structure between Ni and Mo (marked by ♦).[39] Meanwhile, we can infer the enlargement of interlayer spacing with reference to Bragg's law.[41] It is noteworthy to mention that extremely low intensity peaks (marked by ●) also appeared, which correspond to the MoO_2 phase. With this in mind, Mo deficiency is expected in NiMo, which will be further discussed later. In addition, the XRD patterns of $CoMoO_4$ and NiMo/$CoMoO_4$ are visualized in Figure 1c. Almost all the characteristic peaks are well assigned to β-$CoMoO_4$ (ICSD code no. 760022). Finally, two weak peaks emerged at around 2θ = 14° (marked by *) and 35.7° (marked

https://doi.org/10.1021/acsaem.3c01146
ACS Appl. Energy Mater. 2023, 6, 7658−7671

by ■), which are attributed to α-$CoMoO_4$ and MoO_3, respectively. It can be concluded that the designed heterostructure is almost a single-phase β-$CoMoO_4$.

At this point, it might be useful to note that $CoMoO_4$ occurs in multiple phases: the low-temperature α-phase, the high-temperature β-phase, the high-pressure hp-phase, and the hydrate phase.[42] The α-phase $CoMoO_4$ resides in the monoclinic space group $C2/m$ (no. 12). The β-phase crystallizes in the same space group but is subtly different from the α-phase due to the tetrahedral coordination of the Mo^{6+} ions as opposed to an octahedral environment observed for the α-phase. The calcination conducted on the Co−Mo precursor induces the phase transition from α-phase to β-phase.[43] Although there are plenty of experimental publications discussing the difference between these two phases, the transition of $\alpha \rightarrow \beta$ at room temperature after some time makes it a bit challenging to posit a claim on whether the prepared materials are metastable or not. To avoid any confusion, we repeated the XRD analysis on the prepared materials after 4 months and did not observe any phase transition. Therefore, it can be concluded that the β-phase $CoMoO_4$ fabricated in this study is metastable, wherein the transition is kinetically hindered.

The morphology of the catalysts was characterized by FE-SEM. The SEM image of NiMo before the calcination step is demonstrated in Figure 2a, which shows highly agglomerated NPs with an estimated size of <20 nm. Meanwhile, both SEM micrographs of NiMo before and after heat treatment can be viewed in Figure S1. However, the size of these sponge-like agglomerated NPs cannot be easily determined. The EDS elemental mapping and the corresponding elemental spectrum display an even distribution of Ni and Mo over the entire batch of the sample (refer to Figure S2a). The atomic ratio of Ni/Mo was determined to be 4:1 from various spots of the sample batch. It should be considered that the nominal composition of Ni/Mo from initial precursors was 3:1. Nonetheless, the XRD patterns confirmed the presence of MoO_2 besides NiMo alloy, implying Mo deficiency.

The SEM photographs of pristine $CoMoO_4$ and the composite, NiMo/$CoMoO_4$, on NF can be observed in Figure 2b,c. The SEM image of pristine $CoMoO_4$ showcases two distinct morphologies of interwoven nanorods and nanoflowers (high-magnification image in the inset of Figure 2b,c), which are evenly distributed on the backbone of NF (refer to Figure S3). The building blocks of both structures are nanosheets joined to one another either in a one-dimensional (1D) orientation to construct the nanorods or in a circular orientation to develop the nanoflowers. The average thickness of nanosheets can vary from 20 to 60 nm. Similar structures can be seen from the SEM micrographs of NiMo/$CoMoO_4$ grown on NF, except that the size of nanoflowers became smaller compared to those of pristine $CoMoO_4$, and most of the long nanorods transformed into much shorter pieces (shown in Figure 2c). The nanoflowers in NiMo/$CoMoO_4$ wound around the broken rods, creating a porous area on the substrate. The porous structure can provide a large surface area for electrochemical reactions and accelerate the transportation of electrolyte ions, elevating the rate of alkaline HER.[22] The EDS mapping of $CoMoO_4$ and NiMo/$CoMoO_4$, shown in Figure S2b,c confirmed the presence of their constituent elements and their uniform dispersion over the NF template.

To further interpret the crystal structure, morphology, and defects of the as-obtained materials, TEM, HR-TEM, SAED, and HAADF−STEM were utilized. As can be seen from Figure S4a, the well-dispersed NPs of NiMo before calcination are less than 10 nm in size. The low crystallinity of NPs is verified by the SAED image, which is in accordance with the amorphous XRD pattern (shown in Figure 1b). The TEM photographs of NiMo after heat treatment, on the other hand, illustrate a dramatic change in terms of crystallinity; the amorphous NPs transformed into highly crystalline particles with an average size of ∼13 nm (see Figure S4b). The HR-TEM image of heat-treated NiMo exhibits clear lattice fringes with an interplanar distance (d) of 0.217 nm which can be assigned to partial Mo incorporation into the crystal structure of Ni. It is worthy of note that the d-spacing of Ni(111) is 0.202 nm, which can be enlarged with the introduction of a heteroatom like Mo. The result accords with the XRD pattern, showing a noticeable peak shift in the direction of lower 2θ values (refer to XRD interpretation). A similar observation was documented by Yang et al.[39]

Figure 2d depicts the TEM images of pristine $CoMoO_4$ scratched off from NF. $CoMoO_4$ consists of smooth 1D nanorods with an average diameter of ∼135 nm and a length of up to micrometers. The HR-TEM photographs exhibit two lattice spacings of 0.34 nm (green square) and 0.27 nm (red square), which can be well indexed to 220 and 022 planes of monoclinic $CoMoO_4$. The blurry lattice fringes shown in Figure 2d (3rd image from the left to right, shown with the enclosed white-dotted area) demonstrate the existence of atomic structure distortion on the edges of the nanorods, which might have originated from the oxygen atom deficiencies.[29] The TEM micrographs of NiMo/$CoMoO_4$ can be visualized in Figure 2e which are mostly composed of nanosheets. The interplanar spacings of 0.46 and 0.38 nm are consistent with the respective crystalline planes of $CoMoO_4(\bar{2}01)$ and $CoMoO_4(021)$. Interestingly, two distinguishable lattice fringes with d-spacings of 0.217 nm were found, which can be attributed to the presence of NiMo NPs in the hybrid. To clarify this, metallic Ni(111) possesses a d-spacing of 0.202 nm. Once a solid solution between Ni and Mo is created, the resulting interplanar spacing enlarges from 0.202 to 0.217 nm. It must be highlighted that there is a tight interface between NiMo NPs with $CoMoO_4$ nanosheets, forming a heterostructure (the blue line shown in Figure 2e, 3rd image from left to right) to encourage the charge transfer. Meanwhile, the structure distortion can be discerned in Figure 2e (3rd and 4th images from left to right, shown with the enclosed white-dotted area), stemming from oxygen vacancies. More importantly, the oxygen deficiencies are located both on the surface and in the internal structure of NiMo/$CoMoO_4$, presenting a higher defect concentration compared to that of pristine $CoMoO_4$, as evidenced in similar studies.[29] The observation could be attributed to the formation of oxygen bridging between two components through Ni−O−Co and/or Ni−O−Mo, which will be clarified in more detail later. The inset images of Figure 2d,e illustrate the SAED patterns of both samples of $CoMoO_4$ and NiMo/$CoMoO_4$ along the zone axes $[1285]$ and $[3\bar{5}0]$, respectively, verifying the formation of a monoclinic $CoMoO_4$ structure. Finally, the HAADF−STEM image taken from NiMo/$CoMoO_4$ revealed that Co, Mo, Ni, and O elements are dispersed evenly on the nanorod (shown in Figure 2f).

XPS was utilized to get further insights into the surface chemistry and oxidation states of the prepared catalysts. The broad scan survey spectra verify the existence of expected

https://doi.org/10.1021/acsaem.3c01146
ACS Appl. Energy Mater. 2023, 6, 7658−7671

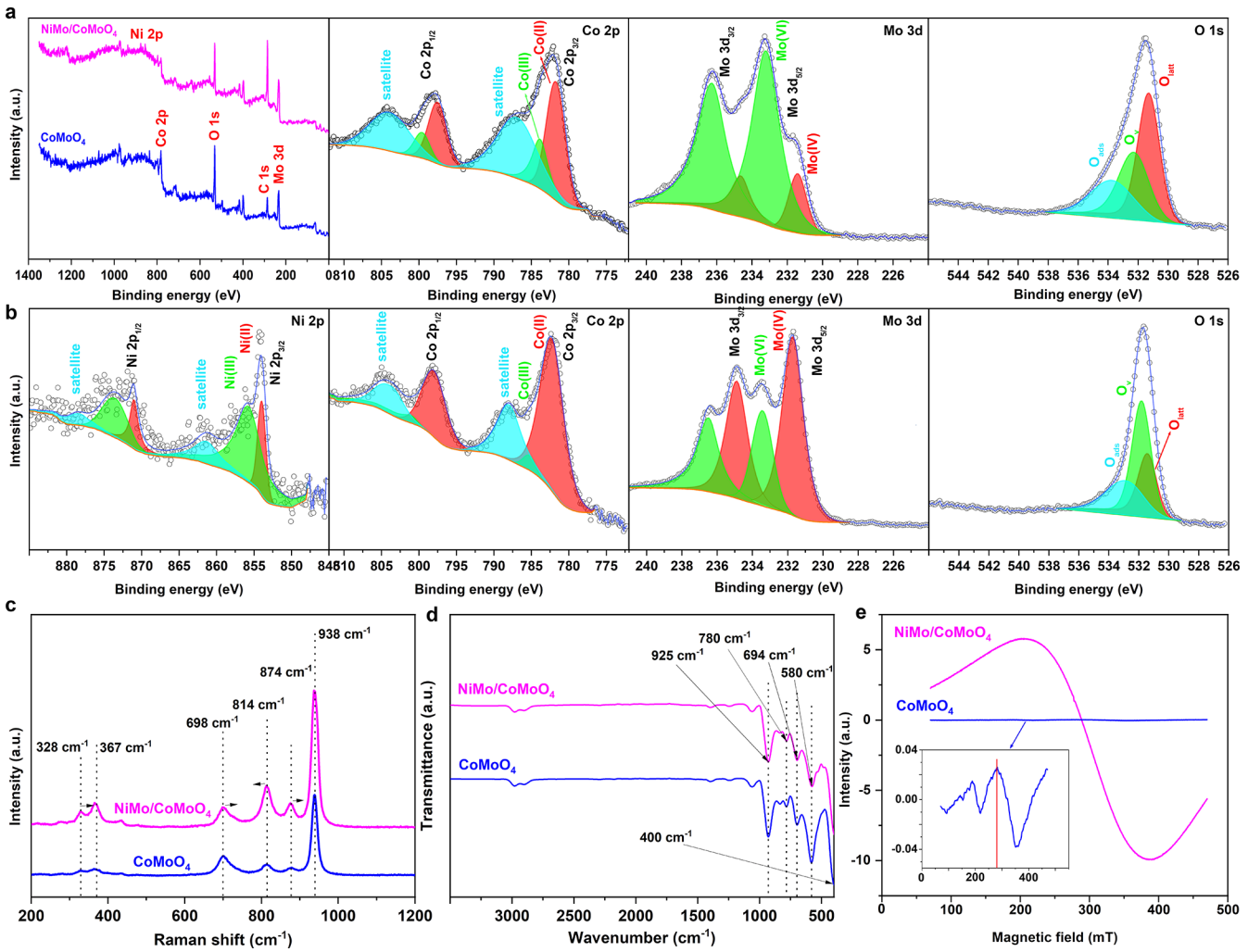


Figure 3. Spectroscopic characterizations of the samples. (a) From left to right, XPS survey spectra of $CoMoO_4$ and $NiMo/CoMoO_4$, and of Co 2p, Mo 3d, and O 1s for $CoMoO_4$, (b) from left to right, XPS spectra of Ni 2p, Co 2p, Mo 3d, and O 1s for $NiMo/CoMoO_4$, (c) Raman spectra, (d) FT-IR spectra, and (e) X-band EPR spectra.

elements in each sample (Figure 3a, 1st panel from left to right). For the NiMo sample (depicted in Figure S5), the Mo 3d spectrum displays two sets of doublets, one at lower BEs, 229.5 and 233.2 eV, and the other pair at higher BEs, 231.5 and 234.8 eV. According to the literature, the former pair belongs to Mo(IV) and the latter pair corresponds to Mo(VI).[7,39] In addition, Figure S5 shows XPS spectra for Ni 2p composed of two doublets of $2p_{1/2}$ and $2p_{3/2}$ as well as their satellite peaks, which were perfectly fitted to Ni(II) and Ni(III).[44] Moreover, the O 1s XPS spectra demonstrate three peaks, indicating the oxidized species on the surface.

For pristine $CoMoO_4$, the deconvolution of the Co 2p region disclosed two main doublet pairs at 781.78, 797.58 eV and 783.88, 799.68 eV alongside their satellites corresponding to Co $2p_{3/2}$ and Co $2p_{1/2}$, indicating the oxidation states of Co(II) and Co(III), respectively.[44,45] The core level Mo 3d XPS spectrum for $CoMoO_4$ exhibited Mo(IV) at BEs centered at ca. 231.38 and 234.6 eV as well as Mo(VI) at ca. 233.2 and 236.28 eV (Figure 3a).[17]

It is evident that the observed XPS spectra of Co 2p and Mo 3d for the $NiMo/CoMoO_4$ sample (Figure 3b) slightly shifted to higher BEs—blue shift—compared with pristine $CoMoO_4$, indicating that the electron density of $CoMoO_4$ was adjusted with the addition of NiMo. This phenomenon confirms that there is an electron transfer between the two constituent components in the hybrid catalyst, from Co and/or Mo sites to Ni sites through oxygen bridging Ni−O−Co and/or Ni−O−Mo, resulting in lower electron density in Co and higher electron density in Ni sites. The deconvoluted Ni 2p spectrum $NiMo/CoMoO_4$ revealed that the two oxidation states of Ni(II) and Ni(III) are present in the hybrid sample; compared with NiMo, their BEs shifted to lower values. This finding confirms the electron transfer from $CoMoO_4$ to NiMo in the hybrid catalyst. The atomic proportions of both Mo and Co decrease in the hybrid catalyst (6.01% for Mo and 3.21% for Co) compared to those of pristine $CoMoO_4$ (8.57% for Mo and 6.91% for Co), further substantiating the electron transfer within the components via oxygen bonding.[21,46−48]

To quantify the concentration of oxygen vacancies in pristine $CoMoO_4$ and the hybrid $NiMo/CoMoO_4$, the O 1s spectra for both samples were fitted. The emerged three peaks for $CoMoO_4$ at BEs of ca. 531.28, 532.28, and 533.76 eV were ascribed to the metal−oxygen bonding or lattice oxygen (O_{latt}), the representative peak of oxygen vacancy (O_v), and adsorbed hydroxyl groups (O_{ads}) on the surface, respectively.[29] The three peaks of O 1s for the hybrid catalyst appeared at low BEs. The ratio of O_v/O_{latt} for these two materials was estimated to be 0.69 for pristine $CoMoO_4$ and 1.84 for $NiMo/CoMoO_4$,

https://doi.org/10.1021/acsaem.3c01146
ACS Appl. Energy Mater. 2023, 6, 7658−7671

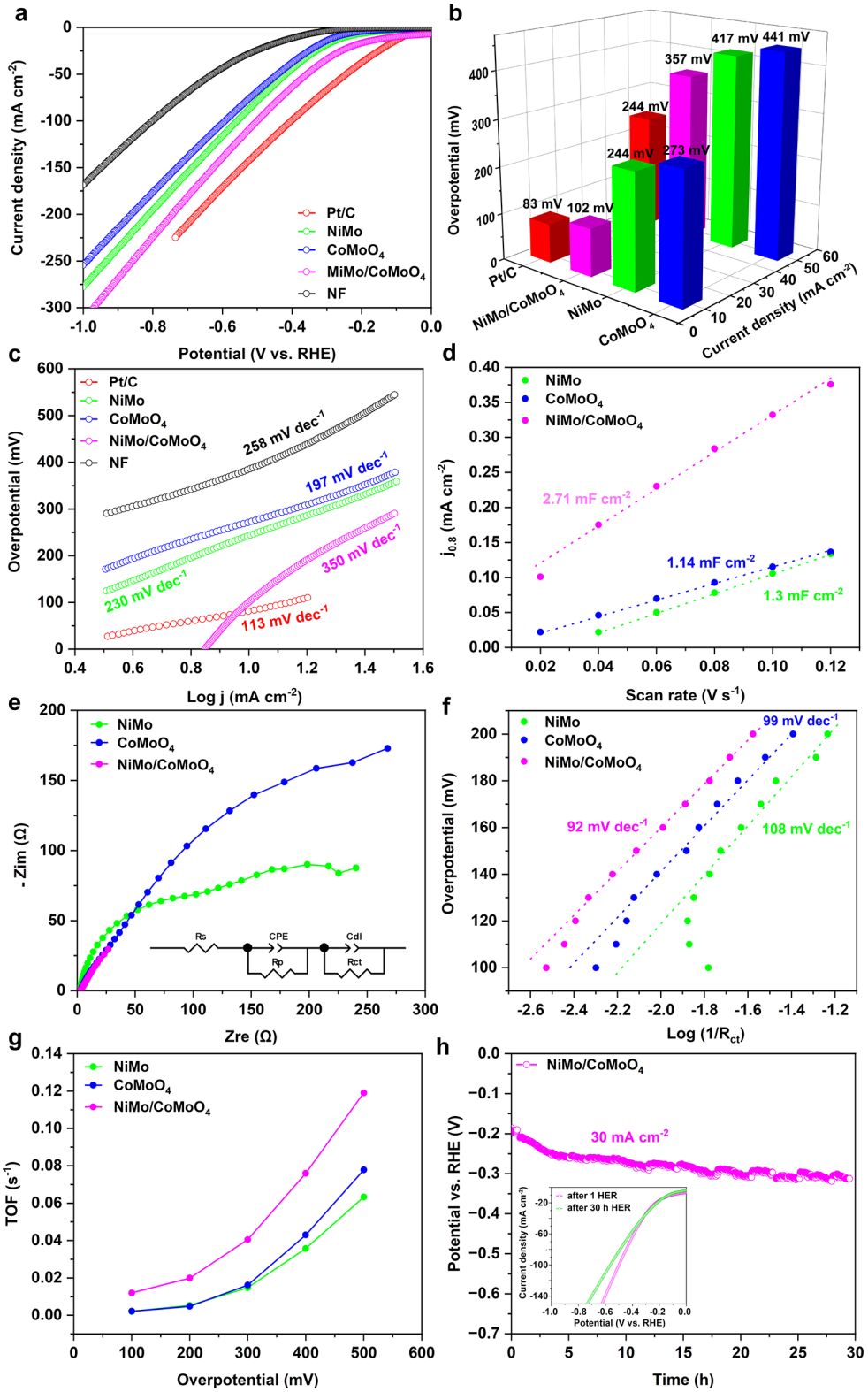


Figure 4. Electrocatalytic hydrogen evolution performances in 1.0 M KOH. (a) HER polarization curves of the samples, (b) 3D bar graphs of overpotentials at 10 and 50 mA cm^{-2}, (c) HER Tafel plots obtained by polarization curves, (d) capacitive current density versus scan rate curves for ECSA measurements, (e) EIS spectra recorded at 0 V versus RHE, (f) HER Tafel plots derived from EIS experiments, (g) TOF (s^{-1}) versus overpotential (mV), and (h) long-term HER durability test of $NiMo/CoMoO_4$ at an applied current density of 30 mA cm^{-2} (inset: HER polarization curves of $NiMo/CoMoO_4$ before and after long-term HER).

implying a significant increase in the oxygen vacancy content on the surface after coupling $CoMoO_4$ and NiMo under heat treatment. By this concept, the engineered oxygen vacancy-confined $NiMo/CoMoO_4$ heterostructure is expected to be a good catalyst for the adsorption of water molecules and subsequently hydrogen reduction.

https://doi.org/10.1021/acsaem.3c01146
ACS Appl. Energy Mater. 2023, 6, 7658−7671

The structural changes between pristine $CoMoO_4$ and NiMo/$CoMoO_4$ were inspected by Raman spectroscopy (Figure 3c). Six characteristic peaks were found in both samples. The sharpest peak located at 938 cm^{-1} denotes the symmetric stretching mode of Mo−O.[49,50] The peaks situated at 874 and 814 cm^{-1} represent asymmetric stretching vibrations of oxygen in O−Mo−O.[29] The band at 698 cm^{-1} was assigned to the symmetric stretching of Co−O−Mo.[49,50] The bands positioned at 367 and 328 cm^{-1} correspond to symmetric torsional vibrations of O−Mo−O.[29,49] For the NiMo/$CoMoO_4$ hybrid, the Raman shifting and peak broadening were observed (Raman shift in Figure S6a), suggesting that original lattice symmetry of $CoMoO_4$ was distorted, which could be attributed to the oxygen defects, inducing a disordered surface.[51]

FT-IR further substantiated the hybridization nature of NiMo/$CoMoO_4$. Figure 3d illustrates the FT-IR spectra for $CoMoO_4$ and NiMo/$CoMoO_4$. The absorption bands at 925 and 780 cm^{-1} denote stretching vibration modes of the O−Mo−O bond.[52−54] The peaks at 694 and 580 cm^{-1} were attributed to the vibrations of the Co−O−Mo and Co−O groups, respectively.[54,55] The band that appeared around 400 cm^{-1} was assigned to the Mo−O and CoO_6 groups of $CoMoO_4$.[55] For the NiMo/$CoMoO_4$ hybrid, all the infrared signals match with those of pristine $CoMoO_4$ sample; however, the hybrid sample exhibits a slight red shift (shown in Figure S6b) around 500−750 cm^{-1}, which suggests that there might be some possible interactions between NiMo and $CoMoO_4$.[54] Besides, this region, which is an indication of metal−oxygen vibration, can be altered by the formation of oxygen defects. The oxygen deficiencies formed in the vicinity of Co−O may weaken the bond strength, giving rise to metal oxide stretching bands shifting to lower wavenumbers.[56]

The X-band EPR measurements were exploited to supply meaningful indications for the generation of oxygen defects within the pristine $CoMoO_4$ and NiMo/$CoMoO_4$ hybrid. Figure 3e shows that both samples have paramagnetic defect centers and that $CoMoO_4$ has two distinct EPR signals at g = 2.4217 and g = 6.377. It has been observed that the g-factor can originate from the existence of Co ions associated with ionized oxygen vacancies. Moreover, the resonance intensity peak of the hybrid sample is much higher than that of pristine $CoMoO_4$, meaning that the metal (Ni/Mo)−oxygen formation masked the emergence of oxygen vacancy defect signals. From the EPR intensity point of view, the defect structures observed in $CoMoO_4$ have been masked by the significant domination of the defects in the NiMo/$CoMoO_4$ hybrid system having a very broad Gaussian EPR peak with the g-factor of g = 2.3193. The dipolar broadening indeed arises from the spin−spin exchange interactions between Mo and Co paramagnetic species and accordingly formed oxygen vacancies in a heterostructured hybrid system. As a result, the heterostructure formation can be further confirmed by the oxygen bridging between Ni/Mo−O−Co.

3.2. Electrochemical Studies. To assess the electrocatalytic ability of the electrodes for the alkaline HER, a typical three-electrode configuration was employed. The HER polarization curves for each sample were obtained through LSV within the reduction potential window. Figure 4a illustrates the electrocatalytic HER performances of the samples, which includes 20 wt % Pt/C and bare NF for comparison. Moreover, the 3D bar graph in Figure 4b presents the overpotential values at 10 and 50 mA cm^{-2} current densities. From this figure, bare NF shows negligible HER behavior (385 and 630 mVat10 and 50 mA cm^{-2}), while Pt/C has superior activity (83 and 244 mV@10 and 50 mA cm^{-2}). Among the prepared materials, the NiMo/$CoMoO_4$ hybrid displayed the highest HER performance with low overpotentials of 102 and 357 mV at 10 and 50 mA cm^{-2} followed by NiMo (244 and 417 mV@10 and 50 mA cm^{-2}) and pristine $CoMoO_4$ (273 and 441 mV@10 and 50 mA cm^{-2}). The tabulated data in Table S1 from the recent reports on similar works containing NiMo indicates that the HER performance of the hybrid catalyst in our study can be compared with those of these catalysts.

The HER kinetics of the catalysts were further examined via the Tafel plots by replotting the polarization curves which can be seen in Figure 4c. As mentioned in the Introduction section, hydrogen evolution in alkaline solutions is governed by two steps of Volmer.

$$H_2O + e^- + {}^* \rightarrow H^* + OH^- \quad \text{(R3)}$$

i.e., water dissociation and adsorption of hydrogen at the catalyst, followed by Heyrovsky

$$H^* + H_2O + e^- \rightarrow {}^* + OH^- + H_2 \quad \text{(R4)}$$

or Tafel

$$2H^* \rightarrow H_2 \quad \text{(R5)}$$

i.e., molecular hydrogen desorption by the combination of H*.[12] According to previous studies, a higher Tafel slope (>120 mV dec^{-1}) suggests that the Volmer step is the rate-determining step, whereas a lower Tafel slope (30 or 40 mV dec^{-1}) implies the Tafel or Heyrovsky step as the rate-determining step.[57] Based on the Tafel slopes calculated from the polarization curves, all the catalysts have similar results, running from 113 mV dec^{-1} for Pt/C to ∼350 mV dec^{-1} for the NiMo/$CoMoO_4$ hybrid. This means that the reaction kinetics is governed by the adsorption and dissociation of water at the catalyst surface.[57] However, the presentation of reaction kinetics via LSV curves becomes a challenge while dealing with highly capacitive materials, such as $CoMoO_4$.[58]

Several factors, such as the applied potential, presence of adsorbates, and mass transport in porous structures, can significantly influence the Tafel slope. It is important to emphasize that experimental observations have shown that the Pt electrode serves as the reference material for the HER, and follows a Tafel path with a slope of 30 mV dec^{-1}.[59] However, as the applied potential increases, the catalyst surface becomes saturated with adsorbed hydrogen atoms, leading to accelerated atom−atom recombination. Consequently, the rate-limiting step shifts to a Volmer path, characterized by a Tafel slope of 120 mV dec^{-1}. In our work, the Pt/C electrode shows a Tafel slope of 113 mV dec^{-1}, verifying its validity with literature in alkaline conditions and approving its rate-limiting step, the Volmer step. In the case of the NiMo/$CoMoO_4$ electrode, the saturated surface covered with adsorbed intermediates brought about the same complication in terms of the Tafel slope, resulting in a higher Tafel value compared to those of the other as-fabricated electrodes. Additionally, non-Faradaic/capacitive currents, iR drops, and conductivity of the catalysts often further complicate the derivation of Tafel slope via LSV.[60] It is worth noting that materials with higher double-layer capacitance contribute more to non-Faradaic reactions, in which, there is no chemical reaction for the charge transfer at the electrode/electrolyte interface.

https://doi.org/10.1021/acsaem.3c01146
ACS Appl. Energy Mater. 2023, 6, 7658−7671

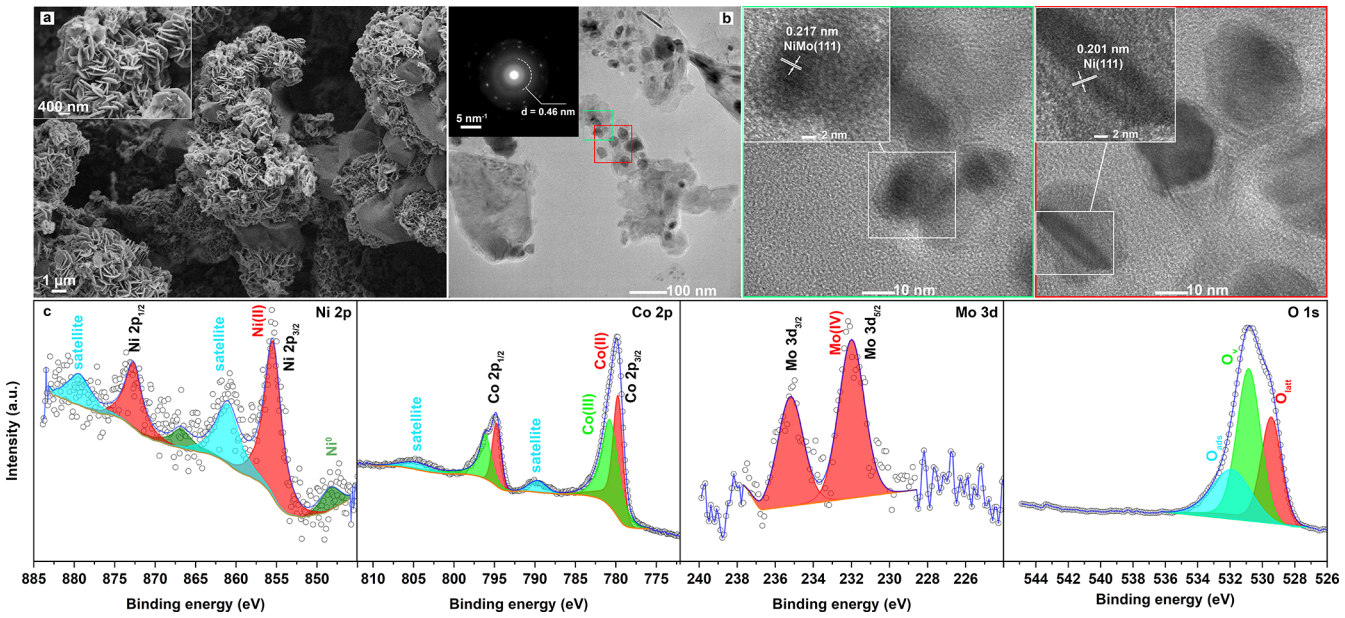


Figure 5. Post-electrolysis characterizations of NiMo/$CoMoO_4$ after long-term HER test. (a) SEM image (inset: high-magnification SEM image), (b) TEM and HR-TEM images (inset: SAED pattern), and (c) XPS Ni 2p, Co 2p, Mo 3d, and O 1s spectra.

To address this issue, Vrubel et al.[61] proposed a new approach to acquire a more reliable Tafel slope for a catalyst through EIS measurements within a certain potential window. In this approach, the Nyquist plots of the catalyst at various overpotentials at regular intervals are obtained, and the slope of overpotentials vs log $(1/R_{ct})$ (where R_{ct} is the charge transfer resistance) gives the relevant precise Tafel slope. The Tafel slope received via this method is accurate as it depends only on the charge transfer capacity of the catalyst and excludes the effect of uncompensated resistance—the resistance exerted by the electrochemical interfaces.[58] Inspired by this study, we determined the Tafel slopes for three materials, namely, NiMo, $CoMoO_4$, and NiMo/$CoMoO_4$. For this, the EIS experiments were performed over the reduction potential ranging from 100 to 200 mV vs RHE with a regular interval of 10 mV (view Figure S7).

The results showed completely different values compared to the Tafel values derived from LSV voltammograms. From Figure 4f, the Tafel slope values demonstrated the following trend: NiMo/$CoMoO_4$ (92 mV dec^{-1}) < $CoMoO_4$ (99 mV dec^{-1}) < NiMo (108 mV dec^{-1}). From more accurate results, we can claim that the hydrogen evolution mechanism on the as-prepared materials proceeds via Volmer–Heyrovsky (120–40 mV dec^{-1}).[62] More importantly, the EIS data recorded at 0.0 V vs RHE exhibited that NiMo possesses the minimum charge transfer resistance (R_{ct} = 244.8 Ω), followed by NiMo/$CoMoO_4$ (R_{ct} = 301.5 Ω), and $CoMoO_4$ (R_{ct} = 463 Ω). All fitted data, based on the equivalent circuit, was tabulated for each sample and can be found in Tables S2–S4. In the representative equivalent circuit (Figure 4e), R_s, R_p, and R_{ct}, respectively, refer to the resistance in solution, resistance from the porosity of the NF substrate, and charge transfer resistance. In addition, to fulfill the non-ideal behavior of the capacitive elements, a constant phase element (CPE) was applied. Similarly, the double-layer capacitance in the interface of the electrode/solution was taken into account through C_{dl}. It should be emphasized that the much larger C_{dl} value of NiMo/$CoMoO_4$ relative to those of NiMo and $CoMoO_4$ accounts for its higher non-Faradaic/capacitive behavior and, in turn, a higher conventional Tafel slope through LSV curves.

To analyze the origin of the electrocatalytic activity of the pristine $CoMoO_4$ and NiMo/$CoMoO_4$—directly grown on NF— their ECSA values were determined through C_{dl}[63] at varying scan rates of 0.02 to 0.12 V s^{-1} (Figure S8). As shown in Figure 4d, the C_{dl} value of NiMo/$CoMoO_4$ increased almost three-fold relative to pristine $CoMoO_4$ (2.71 vs 1.14 mF cm^{-2}). Meanwhile, for NiMo NPs, the C_{dl} was 1.3 mF cm^{-2}. The higher the C_{dl}, the more the exposed active sites on the surface. With this in mind, NiMo/$CoMoO_4$ with a higher C_{dl} value offers a large number of active sites. This is well in line with BET surface area results. The BET surface areas for pristine $CoMoO_4$ and NiMo/$CoMoO_4$ were found to be 7.75 and 22.22 m^2/g, respectively, which exhibit an almost three-fold increase in the surface area in the hybrid catalyst compared with that of $CoMoO_4$. The larger surface area ensures the accessibility of more active sites to promote the adsorption of reactants, accommodates fast charge transfer, encourages the diffusion of electrolyte ions, and thereby elevates the electrocatalytic performance.[18,21] The N_2 adsorption–desorption isotherms can be found in Figure S9. Further details derived from BET analysis are tabulated in Table S5. More importantly, the TOF, which defines the number of molecules that reacted at each available catalytic site per unit time[64] was calculated for the as-fabricated electrodes. In this context, TOF was obtained via the following relation, $\mathrm{TOF} = \frac{j \times A}{\left(2 \times F \times \frac{m}{M}\right)}$, where j stands for current density at a specified overpotential (mA cm^{-2}), A is the surface area of the working electrode (cm^{-2}), F represents the Faraday constant (96485 C mol^{-1}), m denotes the mass loading of the catalyst (g), and M indicates the molecular weight of the catalyst (g mol^{-1}).[65] In general, the TOF measured within the overpotential range of 100–500 mV for the hybrid catalyst was much large than that of $CoMoO_4$. For instance, at a low overpotential of 100 mV, the TOF of NiMo/$CoMoO_4$ obtained was 0.012 s^{-1} which is six times higher than that of

https://doi.org/10.1021/acsaem.3c01146
ACS Appl. Energy Mater. 2023, 6, 7658–7671

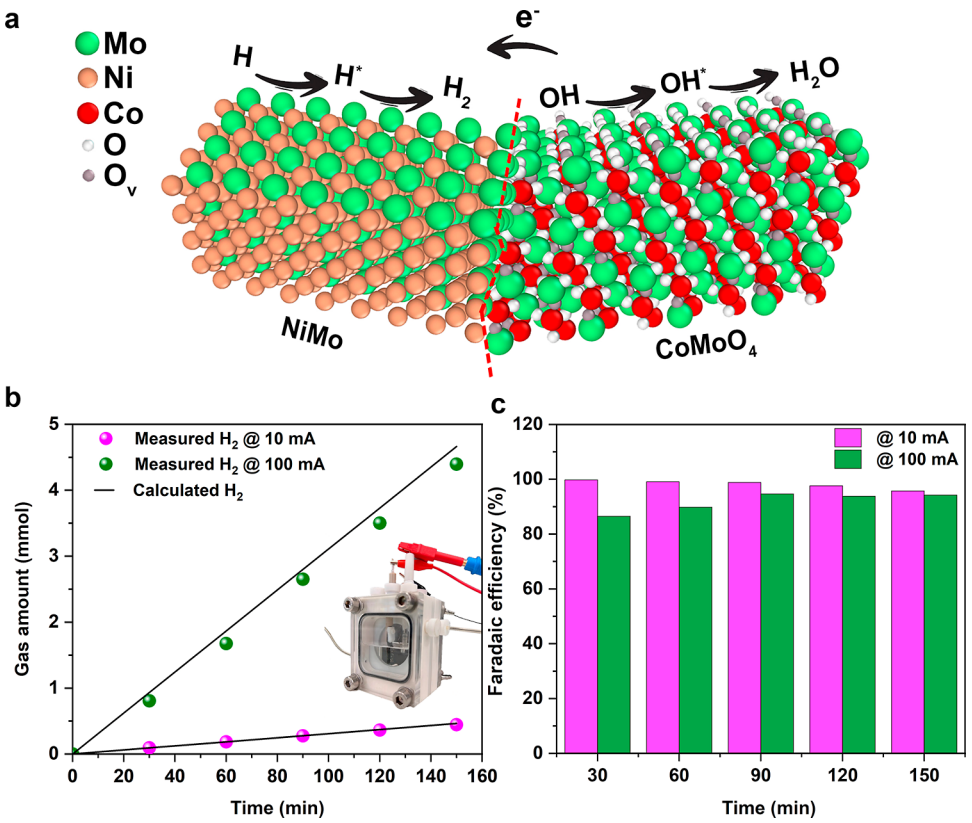


Figure 6. (a) Schematic presentation of the proposed HER mechanism, (b) amount of gas theoretically calculated and experimentally measured for HER using NiMo/$CoMoO_4$ at 10 mA cm^{-2} (inset: home-made electrolysis cell for electrochemical measurements), and (c) quantification of Faradaic efficiency derived from calculated and measured H_2.

$CoMoO_4$, 0.002 s^{-1}. Similarly, at a high overpotential of 500 mV, the TOF of NiMo/$CoMoO_4$ is 0.12 s^{-1} compared to that of $CoMoO_4$, 0.077 s^{-1} (refer to Figure 4g). Finally, the NiMo electrode demonstrated TOF values identical to $CoMoO_4$ within the investigating potential range.

For practical applications of electrocatalysts, long-term durability in the alkaline condition is of high significance. The durability of NiMo/$CoMoO_4$ in 1.0 M KOH was explored at a fixed current density of 30 mA cm^{-2} for 30 h through the chronopotentiometry test. It must be borne in mind that the actual overpotential detected at 30 mA cm^{-2} through the LSV curve is about 283 mV. As shown in Figure 4h, the NiMo/$CoMoO_4$ catalyst exhibits an unsteady-state current during the initial 4 h before reaching a steady-state current, after which it remains quite stable at around 300 mV for the next 26 h. This robust durability could be attributed to the exfoliation of the nanostructures, while the gases are formed and released, bringing about sufficient active surface area on the electrode. The inset picture in Figure 4h depicts the LSV curves before and after 30 h of long-term HER durability. The overpotential at 10 mA cm^{-2} increases from 102 to 163 mV, confirming its competence after 30 h of exposure to 30 mA cm^{-2} reduction current. To investigate the possibility of dissolution and redeposition of the Pt spring—the counter electrode—on the electrode material, we carried out the ICP−MS characterization on the electrolyte solution following long-term HER stability. The results showed that the concentration of Pt inside the solution is infinitesimally low, 0.037 ppb, confirming that it cannot affect the electrocatalysis results. Therefore, the possibility of Pt dissolution and redeposition on the working electrode in this study can be safely ruled out.

3.2.1. Post-electrocatalysis Characterization. To examine the changes after the long-term alkaline HER stability test, we carried out further analyses on the NiMo/$CoMoO_4$ electrode. The SEM image shown in Figure 5a indicates a dramatic change in the topography and morphology of the post-electrolysis sample compared to those of the fresh sample (see Figure 2c). Even though the nanoflowers and nanorods disappeared, the interwoven nanosheets, which were the building blocks of the catalysts, can be observed on the NF substrate. Additionally, the TEM photograph in Figure 5b shows images of nanosheets and NPs, belonging to $CoMoO_4$ and NiMo NPs. The TEM images before and after long-term HER durability are dissimilar in terms of crystallinity, meaning that the degree of crystallinity is reduced after the durability test. However, the two green and red squares delineate two distinctive NPs, one with an interplanar spacing of 0.217 nm, corresponding to NiMo NP, and the other with a *d*-spacing of 0.201 nm, consistent with Ni(111). With this finding, it can be concluded that (i) NiMo NPs are very stable under alkaline conditions even at a high current density of 30 mA cm^{-2} and (ii) Ni with higher oxidation states is reduced to the metallic state during continuous hydrogen evolution.

To identify the oxidation states on the surface, post-stability XPS results (Figure 5c) were analyzed. The Ni 2p core-level spectrum exhibited two doublet peaks with corresponding satellites. The peaks around BEs of 848.5−850, 855.0−855.4, and 860.5−861.2 eV can be assigned to Ni^0, Ni(II), and the Ni shake-up satellite, respectively.[66] The Ni 2p XPS corroborated the results found with HR-TEM, the reduction in the oxidation states of Ni after long-term HER is pronounced. Meanwhile, the atomic proportion of Ni slightly mounted up relative to

https://doi.org/10.1021/acsaem.3c01146
ACS Appl. Energy Mater. 2023, 6, 7658−7671

that of the fresh sample (0.89% → 0.92%), attributed to the emergence of metallic Ni. Interestingly, the Co 2p XPS spectrum demonstrated both Co(II) and Co(III) states. Moreover, the atomic proportion of both oxidation states of Co increases from 3.06 to 3.60% for Co(II) and from 0.15 to 4.77% for Co(III), implying the higher electron density of Co sites after the HER durability test. The meaningful increase in the electron density of Co might be a result of the preference for the adsorption of OH species after the dissociation of water molecules. Furthermore, the signals that appeared at BEs of 779.75 and 780.93 eV revealed the XPS peak shift of Co to lower BEs compared to that in fresh hybrid sample (refer to Figure 3b, Co 2p XPS spectra). In the case of the Mo 3d XPS spectrum, the fitted data showed the presence of only one oxidation state at the BE of 231.91 eV, which can be ascribed to Mo(IV) with a slight shift to a higher BE value. Further, the atomic proportion of Mo 3d drastically declined to 0.16% compared to that of the fresh sample (6.01%). The dramatic decline in the atomic proportion of Mo 3d can likely be due to the complete reduction of Mo(VI) during long-term hydrogen evolution. Finally, the O 1s deconvoluted spectrum exhibited three peaks similar to the fresh sample spectrum. However, the atomic proportion of all three peaks elevated after 30 h HER durability measurement. Based on these observations, it is evident that Ni and Mo are ideal locations for H^+ adsorption and subsequent evolution to molecular H_2, as both metals donate electrons. As a result, localized positive charges appear on the metal surfaces, to neutralize the positive charges, Ni and Mo attract electrons from the surrounding electrolyte and are reduced to lower oxidation states. Conversely, Co atoms in proximity to oxygen vacancies are the preferred sites for OH^- adsorption.

3.3. Proposed Mechanism. Based on the findings, herein, we propose a possible mechanism that can take place during hydrogen evolution electrocatalysis. According to the XPS, HR-TEM, and EPR outcomes, once NiMo and $CoMoO_4$ are combined, a heterostructure can be formed via Ni/Mo−O−Co. To elucidate this point, we must explain that (i) XPS spectra for Ni 2p revealed a peak shift after coupling two components in favor of the higher electron density, (ii) HR-TEM results exhibited oxygen defects in both $CoMoO_4$ and hybrid samples, and (iii) EPR characterizations demonstrated a huge peak for hybrid catalyst due to the presence of Ni/Mo−O. Furthermore, EPR analysis confirmed the presence of oxygen defects within $CoMoO_4$. Therefore, the oxygen vacancy-confined NiMo/$CoMoO_4$ heterostructure was successfully created on NF. The hydrogen evolution in the alkaline solution might occur as follows: once the H_2O molecules dissociate into H and OH (refer to eq R3), metallic NiMo would act as a good proton acceptor; at the same time, the heterostructure with oxygen vacancy modification can be a good adsorber of OH species.

This means the metallic side has a preference for the adsorption of H, whereas the oxygen vacancy-confined side has a preference for the adsorption of OH. In the subsequent step, with the oxygen bridging formation between Ni/Mo−O−Co,[21,46−48] and, in turn, higher electron density on Ni sites—higher electronegativity relative to Co—as a result of electron localization around Ni, the recombination of adsorbed H* to H_2 can take place (refer to eq R5) and be accelerated compared with the individual components of NiMo and pristine $CoMoO_4$ (view the schematic illustration of HER mechanism in Figure 6a). To complement this observation, Zhou et al.[18] performed a similar study to investigate the reaction barrier on the Pt single-atom catalyst coupled with Ni/NiO heterostructure. Based on this work, the kinetics of alkaline HER is mainly dependent on how OH and H bind to the active sites on the catalyst's surface. With the DFT calculations, they proved that metallic Ni has a preference for the adsorption of H, while NiO did not show satisfactory capacity for the adsorption of both OH and H. Conversely, oxygen vacancy-modified NiO displayed elevated ability for the adsorption and stabilization of OH species. With this, the oxygen vacancy in the interface of Ni/NiO can minimize the energy barrier for the splitting of the water molecule into OH and H. Based on their findings, the Pt coupled-Ni/NiO heterostructure demonstrated the strongest H_2O adsorption ability and the largest energy release of −0.09 eV for water dissociation in the Volmer step compared with those of Pt-coupled Ni (0.08 eV) and Pt-coupled NiO (1.01 eV). Eventually, they obtained the optimal value for ΔG_{H^*} for the Pt-coupled Ni/NiO hybrid (−0.07 eV) to improve HER relative to Pt-coupled Ni (−0.38 eV) and Pt-coupled NiO (0.74 eV).

Finally, the quantity of hydrogen evolution on the NiMo/$CoMoO_4$ was determined via gas chromatography through chronopotentiometry at 10 and 100 mA cm^{-2} for 150 min each (Figure 6b). The Faradaic efficiency was estimated using FE = $\frac{n_{exp}}{Q/ZF}$, where n_{exp} stands for the number of moles of H_2 experimentally produced at 10 or 100 mA cm^{-2}, Q (C) refers to the total amount of charge, Z is the number of transferred electrons (i.e., in HER, $Z = 2$), and F is the Faraday's constant (96,485 C mol^{-1}).[15,18] The results can be visualized in Figure 6c. The Faradaic efficiency for H_2 production using the hybrid catalyst was determined to be 100% at 10 mA cm^{-2} and 86−95% at 100 mA cm^{-2}, confirming its high efficiency in generating hydrogen.

4. CONCLUSIONS

In summary, we proved that a competent and stable hydrogen evolution catalyst can be designed by marrying inexpensive components of metallic NiMo and oxygen vacancy-confined $CoMoO_4$ on the NF. The heterostructure formed between two components brought about an electron transfer from $CoMoO_4$ to the NiMo side, resulting in higher electron density on the metallic side. Therefore, following water dissociation into H and OH, the metallic NiMo could preferably adsorb H, whereas oxygen vacancy-modified $CoMoO_4$ might show affinity toward OH species. The ECSA of the NiMo/$CoMoO_4$ hybrid grew almost three-fold compared to that in pristine $CoMoO_4$. Moreover, the BET surface area exhibited similar behavior, indicating a three-fold enlargement of surface area in NiMo/$CoMoO_4$ relative to that in $CoMoO_4$. The NiMo/$CoMoO_4$ reached 10 mA cm^{-2} at a low overpotential of 102 mV for the alkaline HER, approaching the Pt/C performance (83 mV). The HER mechanism was studied via EIS experiments within a reduction window of 100−200 mV, and the hybrid catalyst demonstrated the smallest Tafel slope of 92 mV dec^{-1}, implying hydrogen adsorption (H*) via Volmer and its subsequent desorption (H_2) through Heyrovsky. The Faradaic efficiency for the H_2 production on the fabricated hybrid catalyst confirmed the efficiency as 100% at 10 mA cm^{-2} and 86−95% at 100 mA cm^{-2}. This study presents an affordable, durable, and high-performance catalyst

https://doi.org/10.1021/acsaem.3c01146
ACS Appl. Energy Mater. 2023, 6, 7658−7671

for alkaline hydrogen evolution, which can rival the noble-metal-based catalyst.

■ ASSOCIATED CONTENT

Supporting Information

The Supporting Information is available free of charge at https://pubs.acs.org/doi/10.1021/acsaem.3c01146.

Additional SEM/EDS results and elemental mapping characterizations, TEM/HR-TEM micrographs, XPS spectra, Raman and FT-IR shift, Nyquist plots, fit parameters from the Nyquist plots, CV scans, BET adsorption−desorption isotherms, and additional details from BET analysis (PDF)

■ AUTHOR INFORMATION

Corresponding Author

Umut Aydemir − *Koç University Boron and Advanced Materials Applications and Research Center (KUBAM), Istanbul 34450, Turkey; Department of Chemistry, Koç University, Istanbul 34450, Turkey;* orcid.org/0000-0003-1164-1973; Email: uaydemir@ku.edu.tr

Authors

Ebrahim Sadeghi − *Koç University Boron and Advanced Materials Applications and Research Center (KUBAM), Istanbul 34450, Turkey; Graduate School of Sciences and Engineering, Koç University, Istanbul 34450, Turkey;* orcid.org/0000-0003-0832-0546

Sanaz Chamani − *Koç University Boron and Advanced Materials Applications and Research Center (KUBAM), Istanbul 34450, Turkey*

Emre Erdem − *Faculty of Engineering and Natural Sciences, Materials Science and Nano Engineering, Sabanci University, Istanbul 34956, Turkey; Sabanci University Integrated Manufacturing Technologies Research and Application Center, Composite Technologies Center of Excellence, Istanbul 34906, Turkey*

Naeimeh Sadat Peighambardoust − *Koç University Boron and Advanced Materials Applications and Research Center (KUBAM), Istanbul 34450, Turkey;* orcid.org/0000-0002-2991-5488

Complete contact information is available at: https://pubs.acs.org/10.1021/acsaem.3c01146

Author Contributions

E.S. synthesized the catalysts with the help of S.C. E.S. then performed the chemical characterizations and electrochemical experiments with the support of N.S.P. and S.C. E.E. performed the EPR analysis and helped with its interpretation. U.A. supervised the whole project from synthesis to interpretation of the results.

Notes

The authors declare no competing financial interest.

■ ACKNOWLEDGMENTS

U.A. would like to acknowledge the financial support provided by the Turkish Academy of Sciences—Outstanding Young Scientist Award Program. Likewise, the authors thank Dr. Barış Yağcı, Dr. Amir Motallebzadeh, and Dr. Gülsu Şimşek Franci at Koç University Surface Science and Technology Center (KUYTAM) for their help with characterizations. We would like to express our sincere gratitude to researchers at Koç University Tüpraş Energy Center (KUTEM), especially Dr. Esmail Doustkhah and Muhammed Yusufoğlu for their help with the GC measurements. Finally, we are grateful to Dr. Süleyman Tekmen from Bayburt University Central Research Laboratory (BUMER) and Dr. Gülcan Çorapcıoğlu from Koç University Nanofabrication and Nanocharacterization Center (n^2STAR) for the HR-TEM measurements.

■ REFERENCES

(1) Chaudhari, N. K.; Jin, H.; Kim, B.; Lee, K. Nanostructured materials on 3D nickel foam as electrocatalysts for water splitting. *Nanoscale* **2017**, *9*, 12231−12247.

(2) Xia, H.; Shi, Z.; Gong, C.; He, Y. Recent strategies for activating the basal planes of transition metal dichalcogenides towards hydrogen production. *J. Mater. Chem. A* **2022**, *10*, 19067−19089.

(3) Xiong, B.; Chen, L.; Shi, J. Anion-containing noble-metal-free bifunctional electrocatalysts for overall water splitting. *ACS Catal.* **2018**, *8*, 3688−3707.

(4) Zhang, S. L.; Lu, X. F.; Wu, Z. P.; Luan, D.; Lou, X. W. Engineering Platinum−Cobalt Nano-alloys in Porous Nitrogen-Doped Carbon Nanotubes for Highly Efficient Electrocatalytic Hydrogen Evolution. *Angew. Chem., Int. Ed.* **2021**, *60*, 19068−19073.

(5) Lu, X. F.; Yu, L.; Lou, X. W. Highly crystalline Ni-doped FeP/carbon hollow nanorods as all-pH efficient and durable hydrogen evolving electrocatalysts. *Sci. Adv.* **2019**, *5*, No. eaav6009.

(6) Wang, J.; Yue, X.; Yang, Y.; Sirisomboonchai, S.; Wang, P.; Ma, X.; Abudula, A.; Guan, G. Earth-abundant transition-metal-based bifunctional catalysts for overall electrochemical water splitting: A review. *J. Alloys Compd.* **2020**, *819*, 153346.

(7) Cao, G.-X.; Chen, Z.-J.; Yin, H.; Gan, L.-Y.; Zang, M.-J.; Xu, N.; Wang, P. Investigation of the correlation between the phase structure and activity of Ni−Mo−O derived electrocatalysts for the hydrogen evolution reaction. *J. Mater. Chem. A* **2019**, *7*, 10338−10345.

(8) Kim, J.; Choi, S.; Cho, J.; Kim, S. Y.; Jang, H. W. Toward multicomponent single-atom catalysis for efficient electrochemical energy conversion. *ACS Mater. Au* **2021**, *2*, 1−20.

(9) Wei, R.; Fang, M.; Dong, G.; Ho, J. C. Is platinum a suitable counter electrode material for electrochemical hydrogen evolution reaction? *Sci. Bull.* **2017**, *62*, 971−973.

(10) Liu, Y.; Guo, Y.; Liu, Y.; Wei, Z.; Wang, K.; Shi, Z. A Mini Review on Transition Metal Chalcogenides for Electrocatalytic Water Splitting: Bridging Material Design and Practical Application. *Energy Fuels* **2023**, *37*, 2608−2630.

(11) Kang, Q.; Li, M.; Shi, J.; Lu, Q.; Gao, F. A universal strategy for carbon-supported transition metal phosphides as high-performance bifunctional electrocatalysts towards efficient overall water splitting. *ACS Appl. Mater. Interfaces* **2020**, *12*, 19447−19456.

(12) Sadeghi, E.; Peighambardoust, N. S.; Khatamian, M.; Unal, U.; Aydemir, U. Metal doped layered MgB2 nanoparticles as novel electrocatalysts for water splitting. *Sci. Rep.* **2021**, *11*, 3337.

(13) Sadeghi, E.; Peighambardoust, N. S.; Aydemir, U. Tailoring the Morphology of Cost-Effective Vanadium Diboride Through Cobalt Substitution for Highly Efficient Alkaline Water Oxidation. *Inorg. Chem.* **2021**, *60*, 19457−19466.

(14) Peighambardoust, N. S.; Sadeghi, E.; Mete, B.; Baris Yagci, M.; Aydemir, U. Evaluating electrocatalytic activity of metal-substituted hafnium diboride (Hf1-TMB2; TM = Ni and Co) toward water splitting. *J. Alloys Compd.* **2022**, *905*, 164148.

(15) Sadeghi, E.; Peighambardoust, N. S.; Chamani, S.; Aydemir, U. Designing In Situ Grown Ternary Oxide/2D Ni-BDC MOF Nanocomposites on Nickel Foam as Efficient Electrocatalysts for Electrochemical Water Splitting. *ACS Mater. Au* **2022**, *3*, 143−163.

(16) Zhang, Q.; Zhao, B.; Wang, J.; Qu, C.; Sun, H.; Zhang, K.; Liu, M. High-performance hybrid supercapacitors based on self-supported 3D ultrathin porous quaternary Zn-Ni-Al-Co oxide nanosheets. *Nano Energy* **2016**, *28*, 475−485.

(17) Liu, Z.; Zhan, C.; Peng, L.; Cao, Y.; Chen, Y.; Ding, S.; Xiao, C.; Lai, X.; Li, J.; Wei, S.; et al. A CoMoO 4−Co 2 Mo 3 O 8

heterostructure with valence-rich molybdenum for a high-performance hydrogen evolution reaction in alkaline solution. *J. Mater. Chem. A* **2019**, *7*, 16761−16769.
(18) Zhou, K. L.; Wang, Z.; Han, C. B.; Ke, X.; Wang, C.; Jin, Y.; Zhang, Q.; Liu, J.; Wang, H.; Yan, H. Platinum single-atom catalyst coupled with transition metal/metal oxide heterostructure for accelerating alkaline hydrogen evolution reaction. *Nat. Commun.* **2021**, *12*, 3783.
(19) Tian, H.; Zhang, K.; Feng, X.; Chen, J.; Lou, Y. Self-supported CoMoO 4/NiFe-LDH core−shell nanorods grown on nickel foam for enhanced electrocatalysis of oxygen evolution. *Dalton Trans.* **2022**, *51*, 13762−13770.
(20) Zhang, Z.; Bao, F.; Zhang, Y.; Feng, L.; Ji, Y.; Zhang, H.; Sun, Q.; Feng, S.; Zhao, X.; Liu, X. Formation of hierarchical CoMoO4@MnO2 core−shell nanosheet arrays on nickel foam with markedly enhanced pseudocapacitive properties. *J. Power Sources* **2015**, *296*, 162−168.
(21) Dang, Y.; Wang, G.; Su, G.; Lu, Z.; Wang, Y.; Liu, T.; Pu, X.; Wang, X.; Wu, C.; Song, C.; et al. Rational construction of a Ni/CoMoO4 heterostructure with strong Ni−O−Co bonds for improving multifunctional nanozyme activity. *ACS Nano* **2022**, *16*, 4536−4550.
(22) Liu, M.-C.; Kong, L.-B.; Lu, C.; Ma, X.-J.; Li, X.-M.; Luo, Y.-C.; Kang, L. Design and synthesis of CoMoO 4−NiMoO 4 x H2O bundles with improved electrochemical properties for supercapacitors. *J. Mater. Chem. A* **2013**, *1*, 1380−1387.
(23) Liu, Y.; Xu, P.; Ye, Z.; Cen, T.; Peng, X.; Yuan, D.; Wu, H. P doped CoMoO4/RGO as an efficient hybrid catalyst for hydrogen evolution. *Int. J. Hydrogen Energy* **2020**, *45*, 15157−15165.
(24) Subbaraman, R.; Tripkovic, D.; Chang, K.-C.; Strmcnik, D.; Paulikas, A. P.; Hirunsit, P.; Chan, M.; Greeley, J.; Stamenkovic, V.; Markovic, N. M. Trends in activity for the water electrolyser reactions on 3 d M (Ni, Co, Fe, Mn) hydr (oxy) oxide catalysts. *Nat. Mater.* **2012**, *11*, 550−557.
(25) Sheng, W.; Zhuang, Z.; Gao, M.; Zheng, J.; Chen, J. G.; Yan, Y. Correlating hydrogen oxidation and evolution activity on platinum at different pH with measured hydrogen binding energy. *Nat. Commun.* **2015**, *6*, 5848.
(26) Chen, G.; Wang, T.; Zhang, J.; Liu, P.; Sun, H.; Zhuang, X.; Chen, M.; Feng, X. Accelerated hydrogen evolution kinetics on NiFe-layered double hydroxide electrocatalysts by tailoring water dissociation active sites. *Adv. Mater.* **2018**, *30*, 1706279.
(27) Li, F.; Han, G.-F.; Noh, H.-J.; Jeon, J.-P.; Ahmad, I.; Chen, S.; Yang, C.; Bu, Y.; Fu, Z.; Lu, Y.; et al. Balancing hydrogen adsorption/desorption by orbital modulation for efficient hydrogen evolution catalysis. *Nat. Commun.* **2019**, *10*, 4060.
(28) Huang, J.; Han, J.; Wu, T.; Feng, K.; Yao, T.; Wang, X.; Liu, S.; Zhong, J.; Zhang, Z.; Zhang, Y.; et al. Boosting hydrogen transfer during volmer reaction at oxides/metal nanocomposites for efficient alkaline hydrogen evolution. *ACS Energy Lett.* **2019**, *4*, 3002−3010.
(29) Tao, Y.; Wang, P.; Liang, C.; Yang, N.; Huang, D.; Chen, H.; Luo, Y. Tailoring oxygen vacancies in CoMoO4 for superior lithium storage. *ChemElectroChem* **2020**, *7*, 4815−4821.
(30) Xu, J.; Li, L.; Tang, J.; Dai, L.; Li, X.; Ye, Z.; Luo, J. Powder metallurgy synthesis of porous NiMo alloys as efficient electrocatalysts to enhance the hydrogen evolution reaction. *J. Alloys Compd.* **2021**, *865*, 158901.
(31) Xu, Y.; Yin, S.; Li, C.; Deng, K.; Xue, H.; Li, X.; Wang, H.; Wang, L. Low-ruthenium-content NiRu nanoalloys encapsulated in nitrogen-doped carbon as highly efficient and pH-universal electrocatalysts for the hydrogen evolution reaction. *J. Mater. Chem. A* **2018**, *6*, 1376−1381.
(32) Shen, Y.; Zhou, Y.; Wang, D.; Wu, X.; Li, J.; Xi, J. Nickel−copper alloy encapsulated in graphitic carbon shells as electrocatalysts for hydrogen evolution reaction. *Adv. Energy Mater.* **2018**, *8*, 1701759.
(33) Zhang, J.; Zhou, Y.; Zhang, S.; Li, S.; Hu, Q.; Wang, L.; Wang, L.; Ma, F. Electrochemical preparation and post-treatment of composite porous foam NiZn alloy electrodes with high activity for hydrogen evolution. *Sci. Rep.* **2018**, *8*, 15071.
(34) Gao, W.; Gou, W.; Zhou, X.; Ho, J. C.; Ma, Y.; Qu, Y. Amine-modulated/engineered interfaces of NiMo electrocatalysts for improved hydrogen evolution reaction in alkaline solutions. *ACS Appl. Mater. Interfaces* **2018**, *10*, 1728−1733.
(35) Tian, J.; Cheng, N.; Liu, Q.; Sun, X.; He, Y.; Asiri, A. M. Self-supported NiMo hollow nanorod array: an efficient 3D bifunctional catalytic electrode for overall water splitting. *J. Mater. Chem. A* **2015**, *3*, 20056−20059.
(36) Cao, J.; Li, H.; Pu, J.; Zeng, S.; Liu, L.; Zhang, L.; Luo, F.; Ma, L.; Zhou, K.; Wei, Q. Hierarchical NiMo alloy microtubes on nickel foam as an efficient electrocatalyst for hydrogen evolution reaction. *Int. J. Hydrogen Energy* **2019**, *44*, 24712−24718.
(37) Zhang, L.; Xiong, K.; Nie, Y.; Wang, X.; Liao, J.; Wei, Z. Sputtering nickel-molybdenum nanorods as an excellent hydrogen evolution reaction catalyst. *J. Power Sources* **2015**, *297*, 413−418.
(38) Hu, H.; Fan, Y.; Liu, H. Optimization of NiMo catalyst for hydrogen production in microbial electrolysis cells. *Int. J. Hydrogen Energy* **2010**, *35*, 3227−3233.
(39) Yang, K.; Yao, Q.; Huang, W.; Chen, X.; Lu, Z.-H. Enhanced catalytic activity of NiM (M= Cr, Mo, W) nanoparticles for hydrogen evolution from ammonia borane and hydrazine borane. *Int. J. Hydrogen Energy* **2017**, *42*, 6840−6850.
(40) Chamani, S.; Sadeghi, E.; Unal, U.; Peighambardoust, N. S.; Aydemir, U. Tuning Electrochemical Hydrogen-Evolution Activity of CoMoO4 through Zn Incorporation. *Catalysts* **2023**, *13*, 798.
(41) Vicente, R. A.; Neckel, I. T.; Sankaranarayanan, S. K.; Solla-Gullon, J.; Fernández, P. S. Bragg Coherent Diffraction Imaging for In Situ Studies in Electrocatalysis. *ACS Nano* **2021**, *15*, 6129−6146.
(42) Zhao, J.; Wu, Q.-S.; Wen, M. Temperature-controlled assembly and morphology conversion of $CoMoO_4{\cdot}3/4H_2O$ nano-superstructured grating materials. *J. Mater. Sci.* **2009**, *44*, 6356−6362.
(43) Zagorac, D.; Schön, J. C.; Rosić, M.; Zagorac, J.; Jordanov, D.; Luković, J.; Matović, B. Theoretical and experimental study of structural phases in $CoMoO_4$. *Cryst. Res. Technol.* **2017**, *52*, 1700069.
(44) Du, X.; Ma, G.; Zhang, X. Oxygen vacancy-confined $CoMoO_4$@$CoNiO_2$ nanorod arrays for oxygen evolution with improved performance. *Dalton Trans.* **2019**, *48*, 10116−10121.
(45) Li, Z.; Zheng, M.; Zhao, X.; Yang, J.; Fan, W. Synergistic engineering of architecture and composition in $Ni_xCo_{1-x}MoO_4$@CoMoO 4 nanobrush arrays towards efficient overall water splitting electrocatalysis. *Nanoscale* **2019**, *11*, 22820−22831.
(46) Sun, H.; Li, J.-G.; Lv, L.; Li, Z.; Ao, X.; Xu, C.; Xue, X.; Hong, G.; Wang, C. Engineering hierarchical CoSe/NiFe layered-double-hydroxide nanoarrays as high efficient bifunctional electrocatalyst for overall water splitting. *J. Power Sources* **2019**, *425*, 138−146.
(47) Li, J.-G.; Gu, Y.; Sun, H.; Lv, L.; Li, Z.; Ao, X.; Xue, X.; Hong, G.; Wang, C. Engineering the coupling interface of rhombic dodecahedral NiCoP/C@ FeOOH nanocages toward enhanced water oxidation. *Nanoscale* **2019**, *11*, 19959−19968.
(48) Gao, M.-R.; Liang, J.-X.; Zheng, Y.-R.; Xu, Y.-F.; Jiang, J.; Gao, Q.; Li, J.; Yu, S.-H. An efficient molybdenum disulfide/cobalt diselenide hybrid catalyst for electrochemical hydrogen generation. *Nat. Commun.* **2015**, *6*, 5982.
(49) Rani, B. J.; Swathi, S.; Yuvakkumar, R.; Ravi, G.; Kumar, P.; Babu, E. S.; Alfarraj, S.; Alharbi, S. A.; Velauthapillai, D. Solvothermal synthesis of CoMoO 4 nanostructures for electrochemical applications. *J. Mater. Sci.: Mater. Electron.* **2021**, *32*, 5989−6000.
(50) Veerasubramani, G. K.; Krishnamoorthy, K.; Kim, S. J. Electrochemical performance of an asymmetric supercapacitor based on graphene and cobalt molybdate electrodes. *RSC Adv.* **2015**, *5*, 16319−16327.
(51) Ma, L.; Gao, X.; Zhang, W.; Yuan, H.; Hu, Y.; Zhu, G.; Chen, R.; Chen, T.; Tie, Z.; Liu, J.; et al. Ultrahigh rate capability and ultralong cycling stability of sodium-ion batteries enabled by wrinkled black titania nanosheets with abundant oxygen vacancies. *Nano Energy* **2018**, *53*, 91−96.
(52) Rafieezadeh, M.; Kianfar, A. H. Fabrication of heterojunction ternary Fe3O4/TiO2/CoMoO4 as a magnetic photocatalyst for

https://doi.org/10.1021/acsaem.3c01146
ACS Appl. Energy Mater. 2023, 6, 7658−7671

organic dyes degradation under sunlight irradiation. *J. Photochem. Photobiol., A* **2022**, *423*, 113596.
(53) Pirhashemi, M.; Habibi-Yangjeh, A. Facile fabrication of novel ZnO/CoMoO4 nanocomposites: Highly efficient visible-light-responsive photocatalysts in degradations of different contaminants. *J. Photochem. Photobiol., A* **2018**, *363*, 31−43.
(54) Zhang, X.; Lou, S.; Zeng, Y. Facile fabrication of a novel visible light active g-C3N4-CoMoO4 heterojunction with largely improved photocatalytic performance. *Mater. Lett.* **2020**, *281*, 128661.
(55) Vinothkumar, V.; Abinaya, M.; Chen, S.-M. Ultrasonic assisted preparation of CoMoO4 nanoparticles modified electrochemical sensor for chloramphenicol determination. *J. Solid State Chem.* **2021**, *302*, 122392.
(56) Mansour, S. A.; Farha, A.; Kotkata, M. Sol−Gel Synthesized Co-Doped Anatase TiO 2 Nanoparticles: Structural, Optical, and Magnetic Characterization. *J. Inorg. Organomet. Polym. Mater.* **2019**, *29*, 1375−1382.
(57) Thompson, K.; Choi, J.; Neupane, D.; Mishra, S. R.; Perez, F.; Gupta, R. K. Tuning the electrochemical properties of nanostructured CoMoO4 and NiMoO4 via a facile sulfurization process for overall water splitting and supercapacitors. *Surf. Coat. Technol.* **2021**, *421*, 127435.
(58) Anantharaj, S.; Ede, S. R.; Sakthikumar, K.; Karthick, K.; Mishra, S.; Kundu, S. Recent trends and perspectives in electrochemical water splitting with an emphasis on sulfide, selenide, and phosphide catalysts of Fe, Co, and Ni: a review. *ACS Catal.* **2016**, *6*, 8069−8097.
(59) Li, X.; Hao, X.; Abudula, A.; Guan, G. Nanostructured catalysts for electrochemical water splitting: current state and prospects. *J. Mater. Chem. A* **2016**, *4*, 11973−12000.
(60) Park, K.; Chang, B.-Y.; Hwang, S. Correlation between Tafel analysis and electrochemical impedance spectroscopy by prediction of amperometric response from EIS. *ACS Omega* **2019**, *4*, 19307−19313.
(61) Vrubel, H.; Moehl, T.; Grätzel, M.; Hu, X. Revealing and accelerating slow electron transport in amorphous molybdenum sulphide particles for hydrogen evolution reaction. *Chem. Commun.* **2013**, *49*, 8985−8987.
(62) Akbayrak, M.; Önal, A. M. Binder-free iridium based electrocatalysts: Facile preparation, high activity and outstanding stability for hydrogen evolution reaction in acidic medium. *J. Colloid Interface Sci.* **2020**, *580*, 11−20.
(63) Ramírez, A. M. R.; Heidari, S.; Vergara, A.; Aguilera, M. V. a.; Preuss, P.; Camarada, M. B.; Fischer, A. Rhenium-Based Electrocatalysts for Water Splitting. *ACS Mater. Au* **2023**, *3*, 177−200.
(64) Anantharaj, S.; Karthik, P. E.; Noda, S. The significance of properly reporting turnover frequency in electrocatalysis research. *Angew. Chem., Int. Ed.* **2021**, *60*, 23051−23067.
(65) Mei, Y.; Feng, Y.; Zhang, C.; Zhang, Y.; Qi, Q.; Hu, J. High-Entropy Alloy with Mo-Coordination as Efficient Electrocatalyst for Oxygen Evolution Reaction. *ACS Catal.* **2022**, *12*, 10808−10817.
(66) Tarditi, A. M.; Barroso, N.; Galetti, A. E.; Arrúa, L. A.; Cornaglia, L.; Abello, M. C. XPS study of the surface properties and Ni particle size determination of Ni-supported catalysts. *Surf. Interface Anal.* **2014**, *46*, 521−529.

https://doi.org/10.1021/acsaem.3c01146
ACS Appl. Energy Mater. 2023, 6, 7658−7671